PHYSICAL REVIEW MATERIALS **1**, 061601(R) (2017)

Defect-driven localization crossovers in MBE-grown La-doped $SrSnO_3$ films

Tianqi Wang,[1] Laxman Raju Thoutam,[1] Abhinav Prakash,[1] William Nunn,[1] Greg Haugstad,[2] and Bharat Jalan[1,*]

[1]*Department of Chemical Engineering and Materials Science, University of Minnesota–Twin Cities, Minneapolis, Minnesota 55455, USA*

[2]*Characterization Facility, University of Minnesota, Minneapolis, Minnesota 55455, USA*

(Received 25 August 2017; published 9 November 2017)

Through systematic control of cation stoichiometry using a hybrid molecular beam epitaxy method, we show a crossover from weak to strong localization of electronic carriers in La-doped $SrSnO_3$ films on $LaAlO_3$(001). We demonstrate that substrate-induced dislocations in these films can have a strong influence on the electron phase coherence length resulting in two-dimensional to three-dimensional weak localization crossover. We discuss the correlation between electronic transport, and defects associated with nonstoichiometry and dislocations.

DOI: 10.1103/PhysRevMaterials.1.061601

Doped alkaline-earth stannates ($BaSnO_3$ and $SrSnO_3$) with high room-temperature conductivity and wide band gap are of significant interest for transparent conductors and high-power electronic device applications in addition to channel materials in oxide-based heterostructures [1–6]. Historically, perovskite oxides have shown poor room-temperature mobility owing in part to their band structures, and in part to the presence of intrinsic and extrinsic defects. It was only recently that these materials have witnessed emerging interest for room-temperature electronics due to the discovery of high room-temperature mobility in bulk single crystals [1,2] as well as in thin films of doped $BaSnO_3$ (BSO) [7–12]. Doped $SrSnO_3$ (SSO), on the other hand, is relatively less explored.

The room-temperature phase of SSO has an orthorhombic perovskite structure (space group *Pbnm*) with lattice parameters of $a_0 = 5.709$ Å, $b_0 = 5.703$ Å, and $c_0 = 8.065$ Å and a wide band gap of 3.9–4.5 eV [13–15]. The electronic band structure of SSO is derived from Sn 5*s* and O 2*p* bands, where predominantly Sn 5*s* states form the conduction band minima, thus offering the benefit of a low electron effective mass as compared to the *d*-band perovskite [15–17]. Moreover, the wider band gap and smaller lattice parameter of SSO than that of BSO (and therefore, better lattice matched to many commercially available substrates) makes it a promising material with direct relevance to applications such as high-power devices and transparent electronics. In this context, understanding the role of specific defects on the electronic properties of SSO is of significant interest. There are a number of open questions, however, that are yet to be explored in SSO including the optimal choice of dopant ions, and the relative importance of phonons, ionized impurity scattering including those from point defects, and dislocations. Dislocation and point defect scattering are more significant in thin films due to lattice mismatch between films and substrates, and the influence of the growth parameters on the film's stoichiometry, respectively. Prior works have focused on the synthesis of SSO films using the sol-gel method [18], pulsed laser deposition [19–22], and sputtering [23]. More recently, a low-energy molecular beam epitaxy (MBE) approach has been demonstrated to yield structurally high-quality SSO films but was unsuccessful in producing conducting films despite doping with a large amount of La [13]. Theoretically, La is predicted to be a shallow donor in SSO [17], raising questions on the intrinsic electronic properties of SSO.

To investigate the intrinsic electronic properties of SSO and to identify the roles of cation stoichiometry and dislocations on the electronic transport in doped SSO films, this Rapid Communication focuses on the hybrid MBE growth of La-doped SSO films and temperature-dependent magneto-transport properties providing numerous insights into the role of intrinsic defects on localization physics in SSO films.

We begin by first discussing the structural properties of SSO films on $LaAlO_3$ (LAO)(001), which are critical in establishing a credible case for the electronic properties. Figure 1(a) shows time-dependent reflection high-energy electron diffraction (RHEED) intensity oscillations during the growth of a representative stoichiometric SSO film [Sr/Sn beam equivalent pressure (BEP) ratio $= 8.6 \times 10^{-3}$] indicating that films grew in an atomic layer-by-layer fashion. The inset shows a streaky RHEED pattern after growth with $\frac{1}{2}$-order reflections along $[100]_{LAO}$ azimuth indicating smooth surface morphology. Figure 1(b) shows a wide-angle x-ray diffraction (WAXRD) scan for La-doped SSO (45 nm)/undoped SSO (9 nm)/LAO(001) grown with the same cation flux ratio revealing phase-pure film with an expanded out-of-plane lattice parameter (a_{OP}) of 4.075 Å ± 0.002 Å. This a_{OP} value is higher than the pseudocubic lattice parameter ($c = 4.035$ Å) of bulk SSO indicating this film contains either nonstoichiometric/structural defects/doping or has residual in-plane (biaxial) strain due to incomplete strain relaxation. To examine the role of strain, we performed an off-axis reciprocal space mapping (RSM) scan around the (103) reflection of the same film revealing an out-of-plane lattice parameter value of 4.075 Å ± 0.002 Å, consistent with the results of on-axis WAXRD scans, and an in-plane lattice parameter value of 4.008 ± 0.002 Å [Fig. 1(c)]. We calculate the unstrained lattice parameter of the SSO film using the following equation:

$$a_{\text{unstrained}} = \frac{2\nu a_{\parallel} + (1-\nu)a_{\perp}}{1+\nu},$$

where ν is the Poisson's ratio for bulk SSO (set to a theoretical value of 0.192 [24]), and $a_{\parallel}$ and $a_{\perp}$ are the experimental values of the in-plane and the out-of-plane lattice parameters, respectively, determined from the RSM. The value of $a_{\text{unstrained}}$ was calculated to be 4.053 Å ± 0.002 Å, which is about 0.44% higher than the bulk pseudocubic value as one would expect for

*bjalan@umn.edu

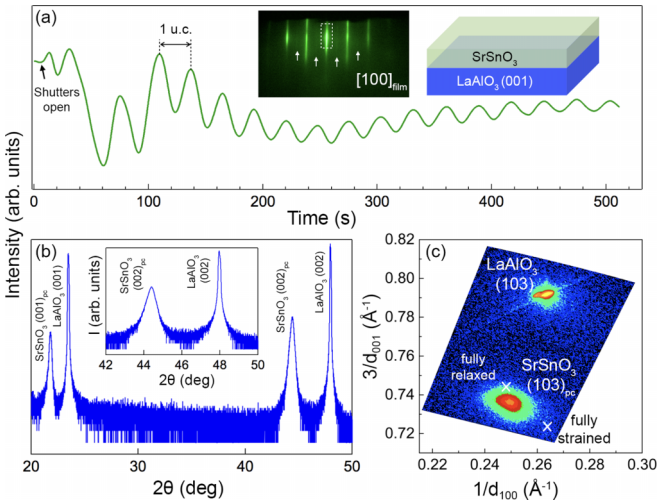

FIG. 1. (a) Time-dependent RHEED intensity oscillations for SSO film grown on LAO(001) substrate grown at a Sr:Sn BEP ratio of 8.6×10^{-3}. The insets show the RHEED pattern along the $[100]_{LAO}$ azimuth after growth, and a schematic of film structure. (b) High-resolution x-ray diffraction for a La-doped SSO (45 nm)/undoped SSO (9 nm)/LAO (001) with an inset showing a close-up around the $(002)_{pc}$ film/substrate peaks. (c) Off-axis RSM taken around the (103) reflection of SSO film on LAO(001). Cross symbol marks the expected positions of a fully strained and a fully relaxed SSO film on LAO(001).

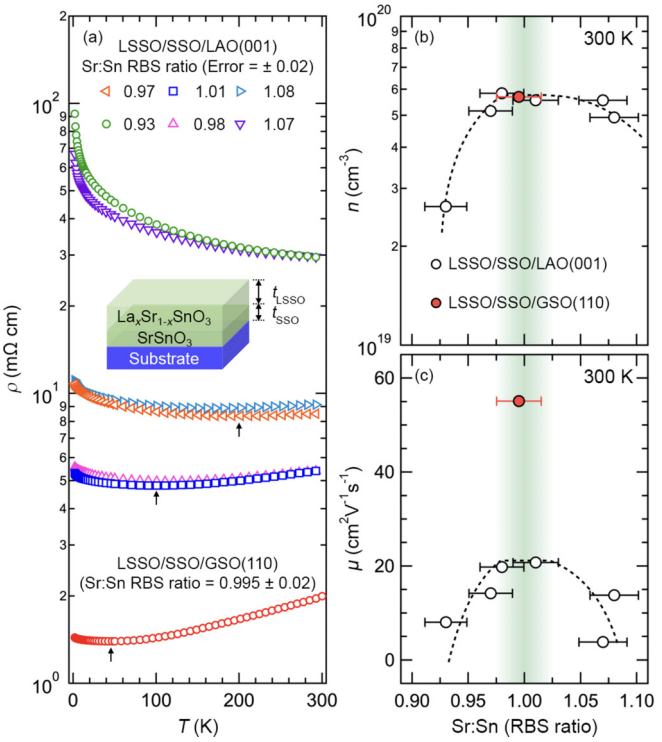

FIG. 2. (a) ρ vs T for La-doped SSO (40 nm)/undoped SSO (8 nm)/GSO(110) and La-doped SSO (45 nm)/undoped SSO (9 nm)/LAO(001) as a function of the Sr/Sn ratio determined from the RBS measurements. Inset shows a schematic of the sample structure. (b) n and (c) μ measured at 300 K as a function of the Sr/Sn RBS ratio.

a nominally stoichiometric composition without any doping. We attribute this increase either to the presence of La dopants in these films or to the error in the theoretical value of the Poisson's ratio. We also note that cation nonstoichiometry may also yield a similar increase in the lattice parameter. To this end, to directly examine the film's cation stoichiometry, we employed the Rutherford backscattering spectrometry (RBS) measurements, which confirmed a nominally stoichiometric composition for these films (see Fig. S1) [25].

As a more sensitive measure of point defects and non-stoichiometry-related defects, we performed electronic transport measurements on La-doped SSO films with a fixed La dopant concentration but varying Sr/Sn ratio. La was used as an n-type dopant and its concentration in the films was kept nominally constant by fixing La-cell temperature and the growth rate. It is expected that nonstoichiometric defects such as Sr or Sn vacancies will compensate for electrons resulting in lower carrier density and mobility similar to what has been shown for La-doped BSO films [26,27]. Figure S1 shows RBS measurements and simulations of La-doped SSO (45 nm)/undoped SSO (9 nm)/LAO(001) grown at a Sr/Sn BEP ratio between 5.7×10^{-3} and 12.0×10^{-3} demonstrating a systematic change in the film's Sr/Sn ratio with changing growth conditions [25]. Importantly, films grown with Sr/Sn BEP ratios of 7.8×10^{-3} and 8.6×10^{-3} showed nominally identical cation stoichiometry with Sr/Sn RBS ratios of 1.01 ± 0.02 and 0.98 ± 0.02, respectively. Figure 2(a) shows T-dependent resistivity (ρ) of these films indicated by their Sr/Sn ratio determined from the RBS measurements. Results from stoichiometric La-doped SSO (40 nm)/undoped SSO (8 nm) films grown on GSO(110) are also included. The corresponding room-temperature values of electron density (n) and mobility (μ) of these films are shown in Figs. 2(b) and 2(c), respectively, as a function of the Sr/Sn ratio determined from the RBS. We first discuss the electronic transport of La-doped SSO films grown on LAO(001). Films grown with Sr/Sn BEP ratios of 7.8×10^{-3} (Sr/Sn RBS ratio $= 1.01 \pm 0.02$) and 8.6×10^{-3} (Sr/Sn RBS ratio $= 0.98 \pm 0.02$) yielded identical room-temperature ρ values $\sim$5.5 mΩ cm, $n \sim 5.5 \times 10^{19}$ cm^{-3}, and $\mu \sim 22$ cm^2 V^{-1} s^{-1} [Figs. 2(a)–2(c)] suggesting nominally identical composition, in agreement with the results of RBS measurements (Fig. S1) [25]. These results revealed that there exists an adsorption-controlled MBE growth window [marked by the green shaded region in Figs. 2(b) and 2(c)], i.e., a range of Sr/Sn BEP ratios where only stoichiometric SSO films grow. We attribute this behavior to the high volatility of hexamethylditin (HMDT) precursor, similar to what has been demonstrated for BSO films [26]. With increasing nonstoichiometry, both n and μ decreased suggesting cation nonstoichiometry can cause carrier localization and enhance scattering regardless of whether they were Sr or Sn vacancies. These results, while attesting to the excellent composition control afforded by the hybrid MBE approach, suggest that the observed and unexplained nonconducting behavior of MBE-grown La-doped SSO films may be due to the presence of nonstoichiometric defects [13]. The presence of non-stoichiometry-related defects also revealed a significant influence on the low-temperature resistivity behavior. Fig-

ure 2(a) shows an upturn in ρ at low temperatures and that this temperature (indicated by black arrows) increases with increasing amounts of nonstoichiometry in La-doped SSO grown on LAO(001). Even the nominally stoichiometric films on LAO(001) showed a small resistivity upturn at $T \approx 100$ K raising a question on the source of disorder in a nominally stoichiometric film. Before we discuss these data, let us turn to the transport results of nominally stoichiometric La-doped SSO (40 nm)/undoped SSO (8 nm)/GSO(110) revealing overall smaller ρ (shown by red open circles) with a significantly higher $\mu \sim 55\,\mathrm{cm^2\,V^{-1}\,s^{-1}}$ at $n \sim 5.7 \times 10^{19}\,\mathrm{cm^{-3}}$. A similar resistivity upturn was observed in this sample but at a much lower temperature $T \approx 45$ K. These results indicate lesser disorder and scattering in stoichiometric film on GSO(110) in addition to raising the same question on the origin of this upturn in nominally stoichiometric films. To this end, we performed a RSM analysis of stoichiometric La-doped SSO (40 nm)/undoped SSO (8 nm)/GSO(110) revealing that these films are mostly strained with some relaxation (see Fig. S2) [25], whereas those grown on LAO(001) substrates were mostly relaxed [see Fig. 1(c)]. These results suggest an important role of dislocations on low-temperature electronic transport. It is also noteworthy that both dislocations and nonstoichiometry-related defects appear to raise the temperature at which resistivity upturn occurs suggesting dislocation cores may also be vacancylike. Future studies should be directed toward examining the composition of dislocation cores.

We next discuss the origin of low-temperature resistivity upturn. Figures 3(a) and 3(d) show ρ vs $\ln T$ plots for the stoichiometric La-doped SSO (45 nm)/undoped SSO (9 nm)/LAO(001) and La-doped SSO (40 nm)/undoped SSO (8 nm)/GSO(110), respectively. Green solid lines represent fits corresponding to the Fermi-liquid behavior, $\rho = \rho_0 + AT^2$ indicating electron-electron scattering as the dominant scattering mechanism at high temperatures $140\,\mathrm{K} < T < 300\,\mathrm{K}$ on both substrates. At low temperatures, ρ vs $\ln T$ revealed a linear dependence (black solid lines), which can be attributed to the quantum corrections. These quantum corrections can be due to weak localization (WL) or electron-electron interaction effects, both of which show a similar behavior and can coexist [28]. Magnetic field (B) can be used to differentiate between these two effects, as WL results in a negative magnetoresistance (MR) and is a low B-field effect [28], whereas electron-electron interactions yield positive MR and are usually dominant at higher B fields [29]. The zero-field resistivity correction due to WL in the two-dimensional (2D) case is given by [28]

$$\sigma(T) = \frac{1}{\rho(T)} = \sigma_0 + p\frac{e^2}{\pi h}\ln\left[\frac{T}{T_0}\right], \qquad (1)$$

where T_0 is the temperature where quantum corrections begin to dominate. σ_0 is a residual conductivity and h is the Planck constant. The value of p depends on the dominant scattering mechanism. The black solid lines in Figs. 3(a) and 3(d) represent a linear fit to the experimental data at low temperatures using Eq. (1), suggesting that 2D WL governs the transport behavior. These fittings also yielded a value of p to be 1.69 and 2.1 for stoichiometric film on LAO(001) and GSO(110), respectively. We will discuss the implications of these values later.

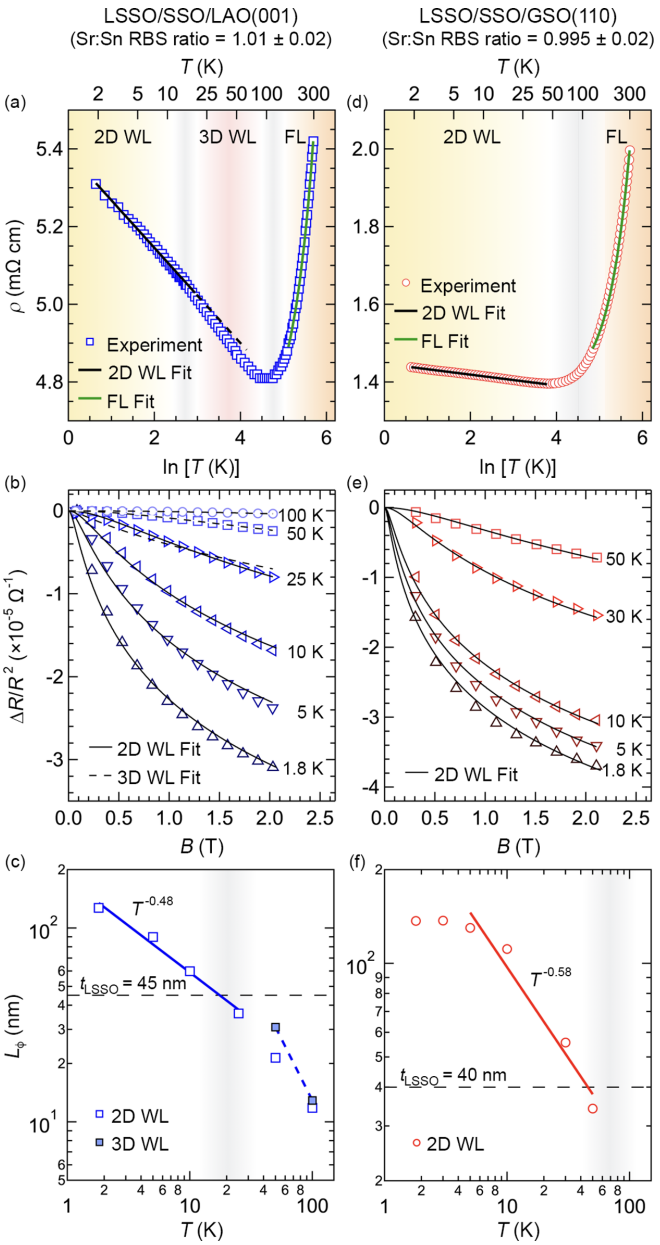

FIG. 3. (a), (d) ρ vs $\ln T$ for stoichiometric films grown on LAO(001) and GSO(110), respectively. Black solid lines are the linear fits using Eq. (1), whereas the green solid lines are fits using the Fermi-liquid model. (b), (e) Normalized MR (symbols) as a function of magnetic field at different temperatures for the same films showing the WL fits with solid lines representing fits using the 2D WL model, whereas dashed lines are fits using the 3D WL model. (c), (f) Temperature dependence of the electron phase coherence length along with the linear fits for films grown on LAO(001) and GSO(110), respectively. The horizontal dashed lines in (c) and (f) indicate the active layer thickness of SSO films.

To examine whether low-temperature ρ is dominated by the WL or electron-electron interaction effect, we performed MR measurements as a function of temperature as shown in Fig. S3 [25]. The MR of both samples shows negative values and its

magnitude increases with decreasing temperature, indicating WL as the dominant effect. However, at higher B-field values, a relative change in MR with B field became smaller, suggesting an increased contribution from electron-electron interaction effect. For this reason, we used low B-field MR values [as illustrated in Figs. 3(b) and 3(e)] to obtain further insights into the WL mechanism such as their dimensionality and phase coherence length of electrons (L_ϕ).

For 2D WL, normalized MR ($\Delta R/R^2$) in the absence of spin-orbit coupling can be written as [30]

$$\frac{\Delta R}{R^2} = \frac{R(B) - R(0)}{R(B)^2} = \frac{e^2}{2\pi^2\hbar}\left[\psi\left(\frac{1}{2}+\frac{1}{x}\right) - \ln\left(\frac{1}{x}\right)\right], \tag{2}$$

where ψ is the digamma function, and $x = 4eBL_\phi^2/\hbar$ where B is magnetic field, L_ϕ is the electron phase coherence length, and $\hbar$ is the reduced Planck constant. It is noteworthy that there is only one fitting parameter, L_ϕ, in this equation. Likewise, for the 3D WL, the above expression is given by [31]

$$\begin{aligned}\frac{\Delta R}{R^2} = \frac{e^2}{2\pi^2\hbar}\sqrt{\frac{eB}{\hbar}}\Bigg\{2\left[\left(2+\frac{1}{x}\right)^{1/2} - \left(\frac{1}{x}\right)^{1/2}\right] \\ - \left(\frac{1}{2}+\frac{1}{x}\right)^{-1/2} - \left(\frac{3}{2}+\frac{1}{x}\right)^{-1/2} \\ + \frac{1}{48}\left(2.03+\frac{1}{x}\right)^{-3/2}\Bigg\}.\end{aligned} \tag{3}$$

We show in Figs. 3(b) and 3(e) the low B-field experimental data and WL fits for the stoichiometric La-doped SSO on LAO(001) and GSO(110), respectively. We first discuss the data from La-doped SSO (45 nm)/undoped SSO (9 nm)/LAO(001) in Fig. 3(b), which shows experimental data (symbols) and fits using both 2D WL [solid black line, Eq. (2)] and three-dimensional (3D) WL models [black dashed line, Eq. (3)]. The 2D WL can describe the experimental MR behavior reasonably well for $1.8\,\mathrm{K} \leqslant T \leqslant 25\,\mathrm{K}$, but fails at higher temperatures, $25\,\mathrm{K} \leqslant T \leqslant 100\,\mathrm{K}$. High-temperature data, on the other hand, can be explained using the 3D WL model. Notably, the temperature where there is a crossover from 2D to 3D WL is also consistent with the deviation of linearity in ρ vs $\ln T$ as illustrated in Fig. 3(a). The extracted values of L_ϕ from these fittings are shown in Fig. 3(c) as a function of temperature. The horizontal dotted line corresponds to the doped layer thickness of 45 nm, again corroborating with our findings of dimensional crossover at $T \simeq 25\,\mathrm{K}$. It is expected that the T dependence of L_ϕ scales as $T^{-p/2}$ where the value of p can allow for determining the types of scattering mechanisms, i.e., $p = 1.0$ and 1.5 for inelastic electron-electron scattering in the 2D and 3D regimes, respectively [32]. As illustrated in Fig. 3(c), analysis of the data yielded a value of p equal to 0.96 in the 2D regime, consistent with electron-electron scattering. Since we only have limited data points in the 3D WL regime to correctly determine the value of p, we can only comment that an increase in the slope is suggestive of electron-electron scattering being the dominant scattering mechanism in the 3D regime as well. We now turn to the discussion of stoichiometric La-doped SSO (40 nm)/undoped SS0 (8 nm)/GSO(110) as illustrated in Figs. 3(e) and 3(f). Figure 3(e) shows $\Delta R/R^2$ vs B plots for $1.8\,\mathrm{K} \leqslant T \leqslant 50\,\mathrm{K}$ revealing excellent agreement between experimental data and 2D WL fits using Eq. (2). This result is further consistent with the observation of linear behavior in ρ vs the $\ln T$ plot as illustrated in Fig. 3(a). The extracted values of L_ϕ from these MR fittings are shown in Fig. 3(f) as a function of temperature. Doped layer thickness, 40 nm, is labeled by the dashed line in agreement with the observed behavior of 2D WL at $T < 50\,\mathrm{K}$. The L_ϕ shows $T^{-0.58}$ dependence yielding a value of $p = 1.16$, indicating inelastic electron-electron scattering as the dominant scattering mechanism. Clearly, the value of p determined from MR analysis and those from the analysis of low temperature ρ vs $\ln T$ differ significantly. We attribute this difference to the presence of electron-electron interaction effect at low temperatures, which is not accounted for in Eq. (1). This effect can also be noticed in Fig. 3(f) showing a saturation in the value of L_ϕ at $T < 5\,\mathrm{K}$ [33].

Notably, the comparison of L_ϕ between these two samples using different substrates suggests that the presence of large density of dislocation in La-doped SSO on LAO leads to a decrease in the value of L_ϕ and therefore results in a dimensional crossover from 2D to 3D WL. To further investigate this point, we show in Fig. S4 transport results from La-doped SSO on LAO(001) grown intentionally with nonstoichiometric composition (Sr : Sn ratio = 1.08), i.e., with increased disorder and are thus expected to have a wider 3D WL regime as a function of temperature [25]. Figure S4 shows consistent results revealing that 2D to 3D WL crossover (Fig. S4) [25] occurs at a lower temperature accompanied by an expanded region for 3D WL when disorder is increased. These results are consistent with the findings of decreased electron phase coherence length due to the presence of disorder associated with both dislocations and point defects. A similar behavior has been previously reported in a ZnO/TiO_x heterostructure [34], n-GaAs [35], owing to the presence of disorder.

Finally, to address the question of what governs the transport in a highly nonstoichiometric sample, we show in Fig. 4(a) the semilogarithmic plot of the zero-field ρ versus $T^{-1/4}$ of a representative La-doped SSO/LAO(001) with a Sr/Sn RBS ratio of 0.93 ± 0.02. The inset shows the Zabrodskii and Zinov'eva analysis [36], an unbiased quantitative technique that compares reduced activation energy [$W = -d(\ln\rho)/d(\ln T)$] vs T on a double-logarithmic plot. The calculated slope (m) of this curve using least-square fit reveals a value of -0.24 ± 0.01 indicating the Mott 3D variable range hopping (VRH) is at play at low temperature $T < 10\,\mathrm{K}$. This result is consistent with the strong positive contribution to the measured MR values at high magnetic field [37,38] [Fig. 4(b)]. With increasing T, MR transitioned to negative values at all magnetic fields, $-9\,T \leqslant B \leqslant +9\,\mathrm{T}$. In the context of hopping transport, the positive MR at high magnetic field can be understood due to the shrinkage of the localized orbital wave function reducing the probability of the overlap between the localized states. In relatively weak magnetic fields, a negative contribution to the MR is due to the suppression of destructive interference between the forward-scattering hopping paths [39]. The temperature dependence suggests that the sample undergoes a weakly localized to a strongly localized transport with decreasing temperature.

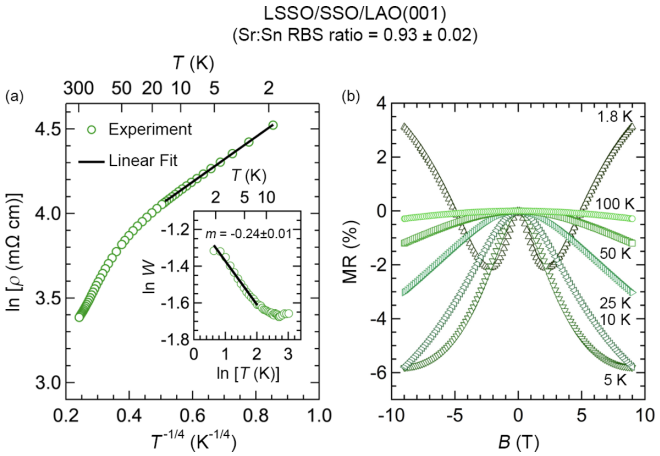

FIG. 4. (a) Logarithmic resistivity versus $T^{-1/4}$ plot for the most nonstoichiometric film (Sr/Ba RBS ratio $= 0.93 \pm 0.02$) grown on LAO(001). The solid black line is the linear fit using the Mott 3D VRH model. Inset shows the temperature dependence of the reduced activation energy using the Zabrodskii and Zinov'eva analysis, yielding a slope, $m = -0.24 \pm 0.01$ indicating the Mott 3D VRH behavior. (b) MR data of the same sample as a function of temperature.

In summary, we have demonstrated the hybrid MBE approach for the growth of phase-pure, stoichiometric, epitaxial SSO films in layer-by-layer growth mode. The use of a highly volatile HMDT precursor facilitated adsorption-controlled growth of SSO with self-regulating cation stoichiometry and yielded record-high room-temperature mobility of $55\,\mathrm{cm^2\,V^{-1}\,s^{-1}}$ in La-doped films on GSO(110). Non-stoichiometry-related defects resulted in lower mobility and a crossover from weak to strong localization of carriers, irrespective of whether they were Sr or Sn vacancies. Substrate-induced dislocations in doped SSO films on LAO(001) yielded dimensional crossover from 2D to 3D WL behaviors. Future investigations on mobility optimization in these materials should account for the disorder caused by the presence of nonstoichiometry as well as dislocations.

This work was primarily supported by National Science Foundation through DMR-1741801, DMR-1607318, and DMR-1410888, and partially by the UMN MRSEC program under Award No. DMR-1420013. Part of this work was supported through the Young Investigator Program of the Air Force Office of Scientific Research (AFOSR) through Grant No. FA9550-16-1-0205. The work also acknowledges partial support from the RDF Fund of the Institute on the Environment (UMN). Parts of this work were carried out at the Minnesota Nano Center and Characterization Facility, University of Minnesota, which receives partial support from NSF through the MRSEC program. T.W. and A.P. would like to acknowledge the support from the UMN Doctoral Dissertation Fellowship.

T.W. and L.R.T. contributed equally to this work.

[1] H. J. Kim, U. Kim, H. M. Kim, T. H. Kim, H. S. Mun, B.-G. Jeon, K. T. Hong, W.-J. Lee, C. Ju, K. H. Kim, and K. Char, Appl. Phys. Exp. **5**, 061102 (2012).

[2] X. Luo, Y. S. Oh, A. Sirenko, P. Gao, T. A. Tyson, K. Char, and S.-W. Cheong, Appl. Phys. Lett. **100**, 172112 (2012).

[3] K. Krishnaswamy, L. Bjaalie, B. Himmetoglu, A. Janotti, L. Gordon, and C. G. Van de Walle, Appl. Phys. Lett. **108**, 083501 (2016).

[4] S. A. Chambers, T. C. Kaspar, A. Prakash, G. Haugstad, and B. Jalan, Appl. Phys. Lett. **108**, 152104 (2016).

[5] S. I. Beigi, F. J. Walker, S. W. Cheong, K. M. Rabe, and C. H. Ahn, APL Mater. **3**, 062510 (2015).

[6] W. J. Lee, H. J. Kim, J. Kang, D. H. Jang, T. H. Kim, J. H. Lee, and K. H. Kim, Annu. Rev. Mater. Res. **47**, 391 (2017).

[7] S. Raghavan, T. Schumann, H. Kim, J. Y. Zhang, T. A. Cain, and S. Stemmer, APL Mater. **4**, 016106 (2016).

[8] Z. Lebens-Higgins, D. O. Scanlon, H. Paik, S. Sallis, Y. Nie, M. Uchida, N. F. Quackenbush, M. J. Wahila, G. E. Sterbinsky, D. A. Arena, J. C. Woicik, D. G. Schlom, and L. F. J. Piper, Phys. Rev. Lett. **116**, 027602 (2016).

[9] A. Prakash, P. Xu, A. Faghaninia, S. Shukla, J. W. A. III, C. S. Lo, and B. Jalan, Nat. Commun. **8**, 15167 (2017).

[10] H. J. Kim, U. Kim, T. H. Kim, J. H. Kim, H. M. Kim, B.-G. Jeon, W.-J. Lee, H. S. Mun, K. T. Hong, J. Yu, K. Char, and K. H. Kim, Phys. Rev. B **86**, 165205 (2012).

[11] K. Ganguly, P. Ambwani, P. Xu, J. S. Jeong, K. A. Mkhoyan, C. Leighton, and B. Jalan, APL Mater. **3**, 062509 (2015).

[12] H. Paik, Z. Chen, E. Lochocki, A. H. Seidner, A. Verma, N. Tanen, J. Park, M. Uchida, S. Shang, B.-C. Zhou, M. Brützam, R. Uecker, Z.-K. Liu, D. Jena, K. M. Shen, D. A. Muller, and D. G. Schlom, arXiv:1711.00496 [cond-mat.mtrl-sci] [APL Materials (to be published)].

[13] T. Schumann, S. Raghavan, K. Ahadi, H. Kim, and S. Stemmer, J. Vac. Sci. Technol., A **34**, 050601 (2016).

[14] B. Bellal, B. Hadjarab, A. Bouguelia, and M. Trari, Theor. Exp. Chem. **45**, 172 (2009).

[15] D. J. Singh, Q. Xu, and K. P. Ong, Appl. Phys. Lett. **104**, 011910 (2014).

[16] K. P. Ong, X. Fan, A. Subedi, M. B. Sullivan, and D. J. Singh, APL Mater. **3**, 062505 (2015).

[17] H. R. Liu, J. H. Yang, H. J. Xiang, X. G. Gong, and S. H. Wei, Appl. Phys. Lett. **102**, 112109 (2013).

[18] K. Nomura, S. Suzuki, Y. Koike, H. Li, A. Okazawa, and N. Kojima, Hyperfine Interact. **237**, 26 (2016).

[19] Q. Liu, J. Dai, X. Zhang, G. Zhu, Z. Liu, and G. Ding, Thin Solid Films **519**, 6059 (2011).

[20] M. C. F. Alves, S. Boursicot, S. Ollivier, V. Bouquet, S. Deputier, A. Perrin, I. T. Weber, A. G. Souza, I. M. G. Santos, and M. G. Viry, Thin Solid Films **519**, 614 (2010).

[21] H. M. Christen, L. A. Boatner, J. D. Budai, M. F. Chisholm, L. A. Gea, D. P. Norton, C. Gerber, and M. Urbanik, Appl. Phys. Lett. **70**, 2147 (1997).

[22] L. Qinzhuang, L. Hong, L. Bing, W. Wei, L. Qiangchun, Z. Yongxing, and D. Jianming, Europhys. Lett. **108**, 37003 (2014).

[23] G. Prathiba, S. Venkatesh, K. K. Bharathi, and H. Kumar, J. Appl. Phys. **109**, 07C320 (2011).

[24] I. R. Shein, V. L. Kozhevnikov, and A. L. Ivanovskii, Solid State Sci. **10**, 217 (2008).

[25] See Supplemental Material at http://link.aps.org/supplemental/10.1103/PhysRevMaterials.1.061601 for the description of experimental methods, Rutherford backscattering spectrometry, x-ray recoprocal space map, and magnetoresistance measurements of SSO films.

[26] A. Prakash, P. Xu, X. Wu, G. Haugstad, X. Wang, and B. Jalan, J. Mater. Chem. C **5**, 5730 (2017).

[27] D. O. Scanlon, Phys. Rev. B **87**, 161201 (2013).

[28] P. A. Lee and T. V. Ramakrishnan, Rev. Mod. Phys. **57**, 287 (1985).

[29] B. L. Altshuler, A. G. Aronov, and P. A. Lee, Phys. Rev. Lett. **44**, 1288 (1980).

[30] C. Van Haesendonck, L. Van den dries, Y. Bruynseraede, and G. Deutscher, Phys. Rev. B **25**, 5090 (1982).

[31] D. V. Baxter, R. Richter, M. L. Trudeau, R. W. Cochrane, and J. O. Stromolsen, J. Phys. France **50**, 1673 (1989).

[32] E. Akkermans and G. Montambaux, *Mesoscopic Physics of Electrons and Photons* (Cambridge University Press, Cambridge, UK, 2007).

[33] J. J. Lin and J. P. Bird, J. Phys.: Condens. Matter **14**, R501 (2002).

[34] D. Saha, P. Misra, S. Bhartiya, M. Gupta, M. P. Joshi, and L. M. Kukreja, Appl. Phys. Lett. **108**, 042109 (2016).

[35] A. M. Gilbertson, A. K. M. Newaz, W. J. Chang, R. Bashir, S. A. Solin, and L. F. Cohen, Appl. Phys. Lett. **95**, 012113 (2009).

[36] A. G. Zabrodskii and K. N. Zinoveva, Pis'ma Zh. Éksp. Teor. Fiz. **37**, 359 (1983) [JETP Lett. **37**, 436 (1983)].

[37] M. E. Gershenson, Y. B. Khavin, A. G. Mikhalchuk, H. M. Bozler, and A. L. Bogdanov, Phys. Rev. Lett. **79**, 725 (1997).

[38] G. M. Minkov, A. V. Germanenko, O. E. Rut, A. A. Sherstobitov, and B. N. Zvonkov, Phys. Rev. B **75**, 235316 (2007).

[39] B. I. Shklovskii and B. Z. Spivak, *Hopping Transport in Solids* (Elsevier, New York, 1991).